
RINGMO-AGENT: A UNIFIED REMOTE SENSING FOUNDATION MODEL FOR MULTI-PLATFORM AND MULTI-MODAL REASONING

Huiyang Hu, Pejin Wang, Yingchao Feng, Kaiwen Wei, Wenxin Yin, Wenhui Diao, Mengyu Wang, Hanbo Bi, Kaiyue Kang, Tong Ling, Kun Fu, Xian Sun

Aerospace Information Research Institute, Chinese Academy of Sciences

School of Electronic, Electrical and Communication Engineering, University of Chinese Academy of Sciences
University of Chinese Academy of Sciences

Key Laboratory of Target Cognition and Application Technology (TCAT)

{huhuiyang22, wangpejin17}mails.ucas.ac.cn

ABSTRACT

Remote sensing (RS) images from multiple modalities and platforms exhibit diverse details due to differences in sensor characteristics and imaging perspectives. Existing vision-language research in RS largely relies on relatively homogeneous data sources. Moreover, they still remain limited to conventional visual perception tasks such as classification or captioning. As a result, these methods fail to serve as a unified and standalone framework capable of effectively handling RS imagery from diverse sources in real-world applications. To address these issues, we propose RingMo-Agent, a model designed to handle multi-modal and multi-platform data that performs perception and reasoning tasks based on user textual instructions. Compared with existing models, RingMo-Agent 1) is supported by a large-scale vision-language dataset named RS-VL3M, comprising over 3 million image-text pairs, spanning optical, SAR, and infrared (IR) modalities collected from both satellite and UAV platforms, covering perception and challenging reasoning tasks; 2) learns modality adaptive representations by incorporating separated embedding layers to construct isolated features for heterogeneous modalities and reduce cross-modal interference; 3) unifies task modeling by introducing task-specific tokens and employing a token-based high-dimensional hidden state decoding mechanism designed for long-horizon spatial tasks. Extensive experiments on various RS vision-language tasks demonstrate that RingMo-Agent not only proves effective in both visual understanding and sophisticated analytical tasks, but also exhibits strong generalizability across different platforms and sensing modalities.

Keywords Foundation model · Multi-modal · Multi-platform · Remote sensing multi-modal large language model · Instruction tuning

1 Introduction

With the remarkable advancements of large language models (LLMs) in semantic understanding and reasoning, vision-language models designed for open-world environments have experienced rapid development [1–3]. Leveraging the capabilities of advanced LLMs such as DeepSeek [4–7], GPT [8, 9], and Llama [10–12], these models are now capable of perceiving complex semantics, conducting multi-turn interactions, and performing context-aware task planning. This evolution marks a significant shift from static perception toward dynamic understanding and autonomous decision-making, thereby enabling broader applications in intelligent interaction and high-level scene reasoning.

Driven by recent advances in these research for natural scenes, the paradigm of vision-language models has gradually extended to RS [13], introducing capabilities such as instruction tuning and joint vision-language modeling into RS image analysis. These efforts have led to the emergence of models that demonstrate promising performance

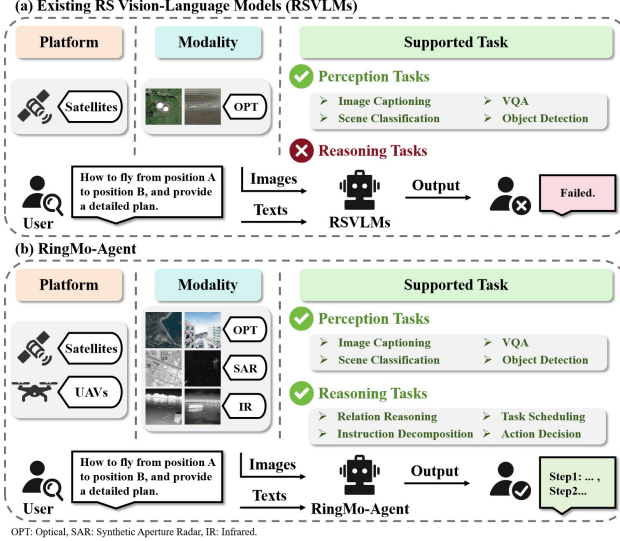


Figure 1: Comparison of RingMo-Agent and most existing RS vision-language models in terms of data platforms, modalities, and supported tasks.

in fundamental RS perception tasks such as object recognition and scene classification [14–24]. However, current vision-language models for RS still suffer from significant limitations:

- **Limitations of single-source modeling in diverse RS data.** Due to variations in data acquisition platforms (e.g., satellites and UAVs) and imaging modalities (e.g., optical, SAR, and infrared), RS data exhibit significant differences in physical characteristics such as spatial resolution, viewing geometry, and spectral response. These heterogeneous properties fundamentally affect the way information is represented in the imagery. However, most existing vision-language models for RS are trained on data from a single modality or platform, limiting their ability to handle the complexity of multi-source data in real-world scenarios. Consequently, these approaches often suffer from poor generalization and limited compatibility in cross-platform and cross-modal applications.
- **Limitations of existing reasoning task paradigms.** Existing RS vision-language research primarily focuses on specific visual perception tasks. However, these tasks remain confined to foundational perception and recognition, with models lacking training in advanced cognitive abilities such as relation reasoning among scene entities and action prediction. Therefore, these models are restricted to narrow applications and struggle to replicate the superior intelligence demonstrated by agent systems in natural scenes when faced with high-level tasks requiring decision-making, as illustrated in Figure 1. This limitation fundamentally stems from the lack of large-scale RS image-text datasets oriented toward complex semantic interactions and reasoning, which restricts the models’ ability to generalize multi-modal knowledge.

To address the aforementioned limitations, we propose RingMo-Agent, a model designed to handle multi-modal and multi-platform data, capable of performing perception and reasoning tasks based on user instructions. **First**, to unleash the potential of vision-language models in intelligent agent applications, we construct a vision-language dataset named RS-VL3M, comprising 3 million image-text pairs across three modalities (optical, SAR, and infrared), two platforms (satellites and UAVs), and eight tasks, as shown in Figure 2. **Second**, we employ a high-dimensional hidden state decoding mechanism based on the special token, which models dynamic trajectory information by focusing on the final-layer hidden representations, enabling support for RS long-horizon reasoning tasks. **Third**, a modality-aware visual encoder with separated embeddings is incorporated to mitigate distribution shifts across different sensing platforms and modalities, supporting robust feature extraction and alignment. **Finally**, unlike previous methods that mainly focus on optical imagery and fundamental perception tasks, RingMo-Agent unifies both perception and reasoning across heterogeneous modalities and platforms, as summarized in Table 1. We further conduct comprehensive comparisons between our proposed model and existing advanced methods on public and self-constructed multi-source RS datasets.

The main contributions can be summarized as follows:

1. We propose RingMo-Agent, a model that supports three sensing modalities and eight task types across two platforms, enabling a unified framework spanning from basic visual perception to advanced reasoning.

Table 1: Comparison of model architectures and capabilities, including LLMs, visual encoders, supported modalities, and task coverage. SAR: Synthetic Aperture Radar, IR: Infrared, IC: Image Captioning, CL: Classification, RR: Relation Reasoning, OD: Object Detection (including visual grounding), ID: Instruction Decomposition, AD: Action Decision, TS: Task Scheduling.

Model	LLM	Visual Encoder	Size	Modalities			Perception Tasks				Reasoning Tasks			
				Optical	SAR	IR	IC	VQA	CL	OD	RR	ID	AD	TS
EarthGPT [14]	LLaMA-2	DINOv2 ViT-L/14, CLIP ConvNeXt-L	-	✓	✓	✓	✓	✓	✓	✓				
Popeye [15]	LLaMA-2 (7B)	DINOv2 ViT-L/14, CLIP ViT-L/14	-	✓	✓						✓			
RS-CapRet [16]	LLaMA-2 (7B)	CLIP ViT-L/14	224	✓			✓							
LHRS-Bot [17]	LLaMA-2 (7B)	CLIP ViT-L/14	224	✓			✓	✓	✓	✓	✓			
SkyEyeGPT [18]	LLaMA-2-Chat (7B)	EVA ViT-G	448	✓			✓	✓	✓	✓	✓			
SkySenseGPT [19]	Vicuna-v1.5	CLIP ViT-L/14	504	✓			✓	✓	✓	✓	✓	✓		✓
GeoChat [20]	Vicuna-v1.5 (7B)	CLIP ViT-L/14	504	✓			✓	✓	✓	✓	✓			
H ² RSVLM [21]	Vicuna-v1.5 (7B)	CLIP ViT-L/14	336	✓			✓	✓	✓	✓	✓			
RingMoGPT [22]	Vicuna-v1.1 (13B)	EVA ViT-G	448	✓			✓	✓	✓	✓	✓			
RGPT [23]	Vicuna (7B/13B)	EVA ViT-G	224	✓			✓	✓	✓	✓	✓			
RS-LLaVA [24]	Vicuna-v1.5 (7B/13B)	CLIP ViT-L/14	336	✓			✓	✓	✓	✓	✓			
RingMo-Agent (ours)	DeepSeekMoE (3B)	SigLIP-SO400M-384	Any	✓	✓	✓	✓	✓	✓	✓	✓	✓	✓	✓

2. We construct RS-VL3M, the first large-scale RS vision-language dataset integrating multi-platform and multi-modal data, with over 3 million image-text pairs. It also includes a high-quality shared multi-modal subset specifically designed for multi-turn dialogue evaluation.
3. RingMo-Agent employs separate embedding layers to mitigate modality-specific distribution shifts and enables joint processing of heterogeneous inputs. It further incorporates a high-dimensional hidden state decoder guided by long-horizon task-specific tokens to model dynamic trajectories through critical hidden representations.

Under the validation, RingMo-Agent shows strong performance across eight RS tasks, outperforming both expert models and generalist models, while exhibiting robust zero-shot generalization.

2 Related works

2.1 Vision-Language Research in Natural Scenes

In recent years, vision-language models have made significant advancements, becoming an essential bridge between visual and language understanding.

Early studies primarily focused on perception-level tasks such as image-text matching, image captioning, and closed-form question answering, emphasizing cross-modal alignment and representation learning between vision and language. For instance, BLIP-2 [25] employs three loss strategies to align visual and textual content, achieving strong performance on VQA and image-text retrieval. InstructBLIP [26] explores a unified instruction-tuning paradigm, where instruction-aware visual feature extraction is employed to accomplish fundamental visual perception tasks. Later works investigated pixel-level tasks including localization, detection, and segmentation. MiniGPT-v2 [27], Kosmos-2 [28], and Shikra [29] explore representing spatial coordinates via natural language. LISA [30] further introduces an embedding-as-mask paradigm, decoding segmentation masks by predicting the hidden representation of a special token.

With the advancement of model capabilities, research exemplified by GPT-4 [9] has gradually expanded to encompass open-ended question answering, visual commonsense reasoning, and multi-turn dialogue tasks, incorporating contextual modeling and knowledge reasoning. The Gemini family [31–33] provides multiple model variants tailored to different computational constraints and application scenarios, demonstrating state-of-the-art performance across multiple dimensions including multi-modal understanding, visual aesthetics, and tool utilization. GPT-4o [34] exhibits superior performance across 50 languages, with substantially enhanced capabilities for processing non-English text. Its lightweight counterpart, GPT-4o Mini [35], offers a more balanced trade-off between performance and computational cost. The Qwen-VL series [36–38] achieves highly competitive results on benchmarks covering coding, mathematics, and general reasoning. Leveraging the low-cost and high-performance characteristics of the DeepSeekMoE [5, 39], DeepSeek-VL2 [40], trained on diverse multi-modal data, is capable of accurately interpreting scientific plots and analyzing various Internet memes.



Figure 2: RingMo-Agent supports perception tasks such as image captioning, object detection, VQA, and scene classification, and reasoning tasks including relation reasoning, instruction decomposition, action decision, and task scheduling. Some tasks are enabled by optical (OPT), SAR, and infrared (IR) modalities.

Recent studies have highlighted autonomous agents built upon LLMs as a promising research direction for achieving human-level decision making, where agent architectures are designed to perceive dynamic environments and translate planning outcomes into executable actions [41]. For example, Reflexion [42] introduces a self-reflection mechanism that enables performance improvement without fine-tuning LLMs, thereby maintaining low computational overhead. HuggingGPT [43] proposes integrating a rich and powerful ecosystem of community-developed AI models, where tasks are planned and appropriate models are selected to execute subtasks and generate responses. Toolformer [44], on the other hand, explores the ability of LLMs to make decisions and autonomously invoke external tools via API interfaces. MetaGPT [45] adopts an assembly line paradigm to organize multiple agents for collaborative cooperation.

Current models are evolving from perception-driven systems to generalist agents with reasoning capabilities, but remain largely focused on natural scenes and struggle with the complexity of RS imagery.

2.2 Vision-Language Research in Remote Sensing

As RS foundation models advance [46, 47], integrating LLMs has become an emerging direction. However, due to data heterogeneity and task diversity, their application in RS remains largely exploratory, with most methods relying on fine-tuning existing architectures.

With works such as RSGPT [23] and RSVG [48] demonstrating that vision-language models can generalize effectively on RS images, research has increasingly focused on the design and training of these models. RemoteCLIP [49] establishes a unified RS vision-language model and validates its effectiveness across downstream tasks such as image classification, image-text retrieval, and object counting. GeoChat [20] introduces a RS vision-language model with multi-task dialogue capabilities, primarily focusing on object existence, as well as attribute judgments such as color and quantity. It also makes preliminary attempts to explore the relationship between object presence and scene semantics. SkyEyeGPT [18] incorporates a UAV video captioning task and investigates the ability of a RS foundation model to jointly learn from both satellite and UAV imagery. RingMoGPT [22] further extend the task scope to include change detection and grounded captioning.

However, existing studies mainly focus on perception tasks using optical imagery, covering only a limited portion of RS data. Recently, EarthGPT [14] incorporates SAR and infrared data to enhance the multi-modal detection capabilities of vision-language models. SkySenseGPT [19] explore the model’s ability to reason about relationships between objects in images. AeroVerse [50] attempts to integrate UAV-based intelligent agent tasks into the vision-language model to explore capabilities in navigation exploration.

Despite recent progress, current RS research remains largely confined to basic perception representation, lacking autonomous decision-making capabilities. Moreover, they predominantly focus on single-platform and single-modal data, which limits their applicability in real-world RS scenarios.

2.3 Tasks and Datasets of Remote Sensing Vision-Language Research

To support the training of RS intelligent systems, numerous vision-language datasets have been developed, most of which are extended from single-modality datasets originally designed for tasks such as object detection, semantic segmentation, image classification, and change detection, and have gradually evolved into large-scale and multi-modal benchmarks.

Early datasets were mostly based on manually annotated image descriptions, with limited scale semantic levels, mainly supporting basic tasks such as VQA and classification, as exemplified by RSVQA [51] and AID [52]. With the expansion of tasks, dataset types and scales have gradually grown. For instance, RemoteCLIP [49] constructs a large-scale caption dataset by applying rule-based methods to RS datasets designed for detection, segmentation, and retrieval, aligning visual and linguistic data. RSVG [48], built upon the optical object detection dataset DIOR [53], conducts attribute analysis on image objects and generates a visual grounding dataset through rule-based processing. RSGPT [23] extends the optical object detection dataset DOTA [54], leveraging expert annotations from RS specialists to develop a comprehensive image captioning dataset.

Several studies have aimed to build large-scale, high-quality RS image-text datasets encompassing diverse task types. XLRs-Bench [55] is designed for optical ultra-high-resolution RS imagery and provides a comprehensive evaluation benchmark encompassing 16 sub-tasks across perception and reasoning. VRSBench [56] provides a large-scale RS vision-language dataset comprising 29,614 images, with annotations covering three key application scenarios: object referring, VQA, and human-verified detailed captions. EarthGPT [14] collects a diverse range of RS data covering five task types and three image modalities, designing different instructions to construct a pretraining dataset. Additionally, models such as GeoChat [20], RingMoGPT [22], and SkySenseGPT [19] leverage constrained LLMs to generate responses for augmented tasks, serving as data for training.

Despite these advancements, there remains a lack of datasets capable of supporting diverse task types, multiple modalities, and various platforms, which is essential for advancing toward generalist intelligent agents.

3 Dataset Construction

3.1 Overall Data Analysis

We construct a large-scale, high-quality RS image-text dataset named RS-VL3M, encompassing images captured by various sensors mounted on different imaging platforms. The dataset features images with diverse resolutions, viewing angles, and imaging mechanisms, totaling over 3 million image-text pairs. It supports two major categories of tasks: reasoning-oriented tasks (task scheduling, action decision, instruction decomposition, and relation reasoning), and perception-oriented tasks (image captioning, object detection, image classification, and VQA), as detailed in Table 2. Furthermore, to enhance the multi-turn dialogue capability of the model under consistent data conditions, we establish a multi-modal dialogue subset based on a shared image pool. This subset enables interactive classification, detection, and captioning tasks on infrared and SAR modalities simultaneously for the same images.

Table 2: The overview of the dataset RS-VL3M, including task types, dataset size, modalities, and image size. $\langle x, x \rangle$ indicates variable image size, representing the range from minimum to maximum.

Task	Dataset	Dataset Size	Modality	Image Size
Task Scheduling	CityNav [57]	32,637	optical	384×384
Action Decision	SkyAgent-Plan3k [50]	3,000	optical	512×512
Instruction Decomposition	ReCon1M-DEC (ours)	27,821	optical	$\langle 135, 1000 \rangle$
Relation Reasoning	FIT-RS [19] ReCon1M-REL (ours)	97,843 125,000	optical optical	512×512 $\langle 135, 1000 \rangle$
Object Detection	DIOR [53] DOTA [54] NWPU VHR-10 [58] SARDet-100k [59] IR-DET (ours)	23,463 108,047 800 116,598 56,353	optical optical optical SAR infrared	800×800 800×800 $\langle 500, 1100 \rangle$ $\langle 190, 1000 \rangle$ $\langle 92, 6912 \rangle$
Image Captioning	UCM-Captions [60] Sydney-Captions [60] RSICD [61] NWPU-Captions [62] SAR-CAP (ours) IR-CAP (ours)	10,500 3,065 54,605 157,500 582,990 281,765	optical optical optical optical SAR infrared	256×256 500×500 224×224 256×256 $\langle 190, 1000 \rangle$ $\langle 92, 6912 \rangle$
Scene Classification	AID [52] NWPU-RESISC45 [63] WHU-RS19 [64] UCMerced-LandUse [65] SAR-CLA (ours) IR-CLA (ours)	10,000 31,500 1,005 2,100 116,597 56,353	optical optical optical optical SAR infrared	600×600 256×256 600×600 256×256 $\langle 190, 1000 \rangle$ $\langle 92, 6912 \rangle$
VQA	RSVQA-HR [51] RSVQA-LR [51]	1,066,316 77,232	optical optical	512×512 256×256

3.2 Dataset Construction for Tasks

In addition to utilizing publicly available datasets directly, we also construct datasets for complex tasks by processing open-source multi-modal data. The overall workflow is illustrated in Figure 3. We extract object-level attribute information from optical, SAR, and infrared images and format the data according to the design requirements of each task. For data usage, to ensure consistent spatial representation, all coordinates are normalized to the range $[0, 999]$. The `[label]` option is provided to indicate the modality branch during training and inference, and is also presented as clickable buttons in the web interface, with possible values `opt`, `sar`, and `ir`. Details of the data for each task category are provided below.

Task Scheduling. This task focuses on trajectory planning for autonomous aerial navigation in complex urban environments based on RS imagery. Given instructions that describe the spatial context surrounding the target location, the model must identify the 3D position of the target based on references to nearby buildings or landmarks, and, given the initial pose of the agent, produce a sequence of 3D waypoints along with corresponding orientation angles. Our task scheduling dataset is derived from CityNav [57] and structured as follows:

- Prompt: $\langle |navigation| \rangle$ You need to formulate a flight plan for a quadcopter based on this map, enabling it to fly over all the buildings and reach the destination. The target location is described as follows: $\langle |description| \rangle$. The 3D coordinates of the landmark are as follows: $\langle |ref| \rangle \langle |landmark| \rangle \langle |/ref| \rangle \langle |pos| \rangle [x_1, y_1, z_1] \langle |/pos| \rangle$. Your starting 3D coordinates and orientation angles are $\langle |pose| \rangle [[x_0, y_0, z_0, \phi_0, \theta_0, \psi_0]] \langle |/pose| \rangle$. You need to provide a series of 3D waypoints and attitude angles for the quadcopter to reach the target location.
- Response: Step 1: Extract basic information as follows: Target: $\langle |target| \rangle$. Landmarks: $\langle |landmark| \rangle$. Surroundings: $\langle |surrounding| \rangle$.
Step 2: Get landmarks position: $\langle |ref| \rangle \langle |landmark| \rangle \langle |/ref| \rangle \langle |pos| \rangle [x_1, y_1, z_1] \langle |/pos| \rangle$.
Step 3: Get target position: $\langle |ref| \rangle \langle |target| \rangle \langle |/ref| \rangle \langle |pos| \rangle [x_2, y_2, z_2] \langle |/pos| \rangle$.
Step 4: Trajectory: $\langle |pose| \rangle [[x_0, y_0, z_0, \phi_0, \theta_0, \psi_0], \dots, [x_n, y_n, z_n, \phi_n, \theta_n, \psi_n]] \langle |/pose| \rangle$.

A set of special tokens is embedded in the prompt: $\langle |navigation| \rangle$ defines the task type. $\langle |ref| \rangle$ and $\langle |/ref| \rangle$ denote the name of a landmark, while $\langle |pos| \rangle$ and $\langle |/pos| \rangle$ indicate its corresponding coordinates. The trajectory is structured using $\langle |pose| \rangle$ and $\langle |/pose| \rangle$ tags, where each pose entry consists of six elements: spatial position (x, y, z) and orientation angles (ϕ, θ, ψ), representing roll, pitch, and yaw respectively. Besides, placeholders such as $\langle |landmark| \rangle$, $\langle |surrounding| \rangle$, and $\langle |target| \rangle$ are used to mark category information (e.g., “Wellington Road”), while $\langle |description| \rangle$ is a placeholder sentence used to describe the spatial surroundings

of the target (e.g., “The row of grayish brown houses on Leslie Road to the left of the gray house at the intersection with Wellington Road”).

Action Decision. This task focuses on fine-grained action decision planning for aerial agents navigating urban environments, bridging visual-language reasoning with control execution. Given the initial and target 3D poses, along with urban map imagery, the model is required to generate a detailed sequence of instructions. Each instruction corresponds to an interpretable motion step (e.g., “go straight,” “slightly turn right”) and is grounded in observable visual cues such as nearby buildings, colors, shapes, or spatial layouts. Our action decision dataset uses data from SkyAgent-Plan3k [50], as exemplified below:

- Prompt: <|decision|>How to fly from position<|pose|>[[$x_0, y_0, z_0, \phi_0, \theta_0, \psi_0$]]<|/pose|> to position<|pose|>[[$x_n, y_n, z_n, \phi_n, \theta_n, \psi_n$]]<|/pose|>, and provide a detailed plan.
- Response: Step1: <description>.
Step2: <description>.
...
Stepn: <description>.

We introduce a special token <|decision|> to specify task semantics. The usage of <|pose|> and <|/pose|> is consistent with the task scheduling dataset. The starting point appears in the first image, and the destination in the last. The output format requires each scene transition to be annotated with a <description> tag, with each step written from the agent perspective in natural language to support human understanding and decision-making.

Instruction Decomposition. This task aims to improve the capability of the model to execute complex, high-level RS commands by breaking them down into a sequence of fine-grained, interpretable sub-tasks. In our setting, the model receives an image alongside a natural language command that may reference specific regions or semantic goals. The model is expected to decompose this input into a structured multi-step reasoning process, including region localization, object detection, relation analysis, and contextual summarization. Our instruction decomposition dataset builds upon the RS relation comprehension dataset ReCon1M [66].

- Prompt: <|decomposition|>Analyze the region <|det|>[[x_1, y_1, x_2, y_2]]<|/det|> of the image.
- Response: Step 1: Locate the target area: The target area locates at the <direction> of the image;
Step 2: Perform object detection: There are N entities in the target area, including: $N_1 <|\text{ref}|><|\text{object}|> <|\text{ref}|><|\text{det}|>[[x_1^1, y_1^1, x_2^1, y_2^1]] <|\text{det}|>, \dots, N_n <|\text{ref}|><|\text{object}|> <|\text{ref}|><|\text{det}|>[[x_1^n, y_1^n, x_2^n, y_2^n]] <|\text{det}|>;
Step 3: Perform relation analysis: There are M relations found: <|ref|><|object|><|ref|><|det|>[[$x_1^1, y_1^1, x_2^1, y_2^1$]]<|det|> is <|rel|><|relation|><|rel|> the <|ref|><|object|><|ref|><|det|>[[$x_1^m, y_1^m, x_2^m, y_2^m$]]<|det|>;
Step 4: Perform context summary: N object types with M interactions.$

As shown above, <direction> has 9 directions, upper, lower, left, right, upper left, upper right, lower left, lower right, and center. N is the total number of detected objects, with N_1 to N_n representing category-wise counts. <|ref|><|object|><|ref|><|det|>[[$x_1^1, y_1^1, x_2^1, y_2^1$]]<|det|> denotes the specific class of objects with spatial location information, where $[x_1^1, y_1^1, x_2^1, y_2^1]$ denote the top-left and bottom-right corners, respectively. <|rel|><|relation|><|rel|> denotes the relationship between the two objects.

Relation Reasoning. This task requires the model to infer the categories of the subject and object and to describe the relationship between them, thereby enabling it to recognize objects in the image and reason about their interactions. Our dataset is derived from the RS instruction-tuning dataset FIT-RS [19] and the RS relation comprehension dataset ReCon1M [66].

- Prompt: <|reasoning|>What is the relationship between <|ref|><|object₁|><|ref|><|det|>[[$x_1^1, y_1^1, x_2^1, y_2^1$]]<|det|> and the object in <|det|>[[$x_1^2, y_1^2, x_2^2, y_2^2$]]<|det|> in the image? And output their categories.
- Response: subject: <|object₁|>, object: <|object₂|>, the <|object₁|> is <|rel|><|relation|><|rel|> the <|object₂|>.

Consistent with other tasks, we define a set of special tokens to explicitly mark different semantic components in both the prompt and response.

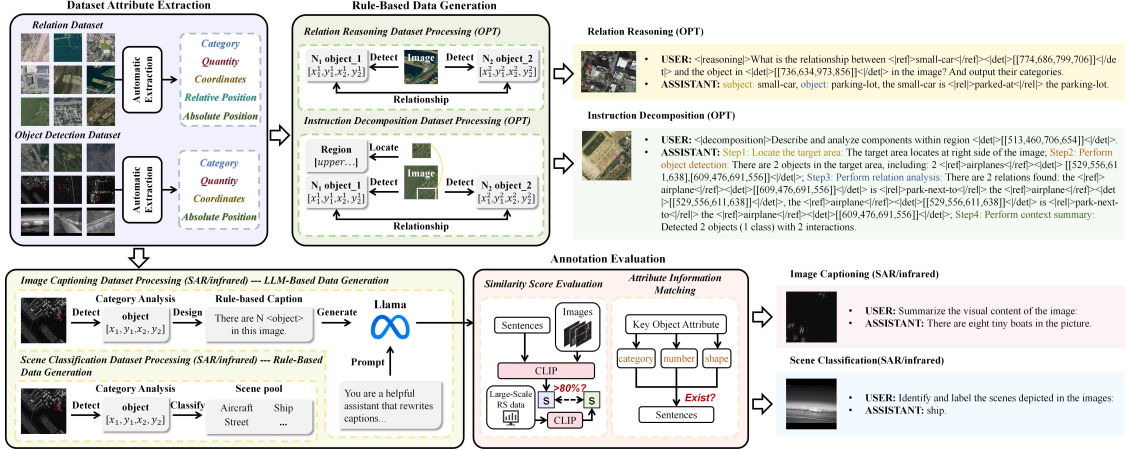


Figure 3: A dataset construction workflow that extracts relevant attributes from existing relation and detection datasets for instruction decomposition, relation reasoning, classification, and captioning tasks.

Object Detection. The optical images are from DIOR [53], DOTA [54], and NWPU VHR-10 [58], SAR images are from SARDet-100k [59], and infrared images are from HIT-UAV [67], Sea shipping [68], Infrared-security [69], Aerial-mancer [70], Double-light-vehicle [71], and Oceanic ship [72].

- Prompt: Detect all objects shown in the remote sensing image and describe using horizontal bounding boxes (HBBs).
- Response: There is/are $M < |\text{ref}| > < \text{object} > < |\text{ref}| > < |\text{det}| > [[x_1^1, y_1^1, x_2^1, y_2^1], \dots, [x_1^M, y_1^M, x_2^M, y_2^M]] < |\text{det}| >$ in the image.

A placeholder $< \text{object} >$ is used to represent category names (e.g., ‘‘ship’’). The use of coordinates follows the same approach as described previously.

Image Captioning. We construct a multi-modal image captioning benchmark using SAR-CAP, IR-CAP, and various optical captioning datasets. The SAR and infrared data are sourced from the same datasets as the object detection task, while optical data is sourced from public datasets [60–62].

Optical captions are often richer due to easier manual annotation, typically describing simple scenes with buildings and vegetation. In contrast, SAR and infrared data demand expert analysis. To address this issue, we first generate rule-based captions for objects in the images using standard templates as illustrated in Figure 3. These captions are then fed as text inputs to Llama3.1 [12], accompanied by carefully designed prompts that constrain the model to enrich the language while preserving three key attributes: the number, shape, and category of objects. The model produces five distinct textual descriptions for each image. We perform automated validation on the generated texts, which consists of similarity score evaluation and attribute information matching. We compute similarity scores between the generated texts and remote sensing images using RemoteCLIP [49], and compare them with benchmark scores obtained from open-source image captioning datasets. Only texts whose similarity scores exceed 80% of the benchmark are retained. For attribute consistency, we further validate the number, shape, and category of the objects described in the texts, allowing for synonymous expressions, and retain only the samples that satisfy all these criteria. This approach effectively ensures the accuracy and consistency of the generated descriptions.

- Prompt: Please provide a short depiction of the picture:
- Response: A single sailboat is present in the scene.

Image Classification. We construct SAR and infrared classification datasets using the same sources as before. For SAR, we adopt the original category definitions, while for infrared data, inconsistent annotations across datasets are addressed by grouping labels into two coarse categories: street scenes and ships. Optical data is sourced from publicly available datasets.

- Prompt: Please output the scene corresponding to the image:
- Response: aircraft.

In our dataset, infrared and SAR images used for detection, captioning, and classification tasks constitute a shared subset, meaning that each image is annotated to support all three tasks. This design enables multi-turn evaluation under consistent visual inputs, while in this study, we validate them as three separate tasks.

VQA. We use public datasets [51] as our training and evaluation benchmarks. These datasets are widely adopted as standard benchmarks for evaluating vision-language models.

- Prompt: Is a small road present? The answer to this question is
- Response: yes.

4 Method

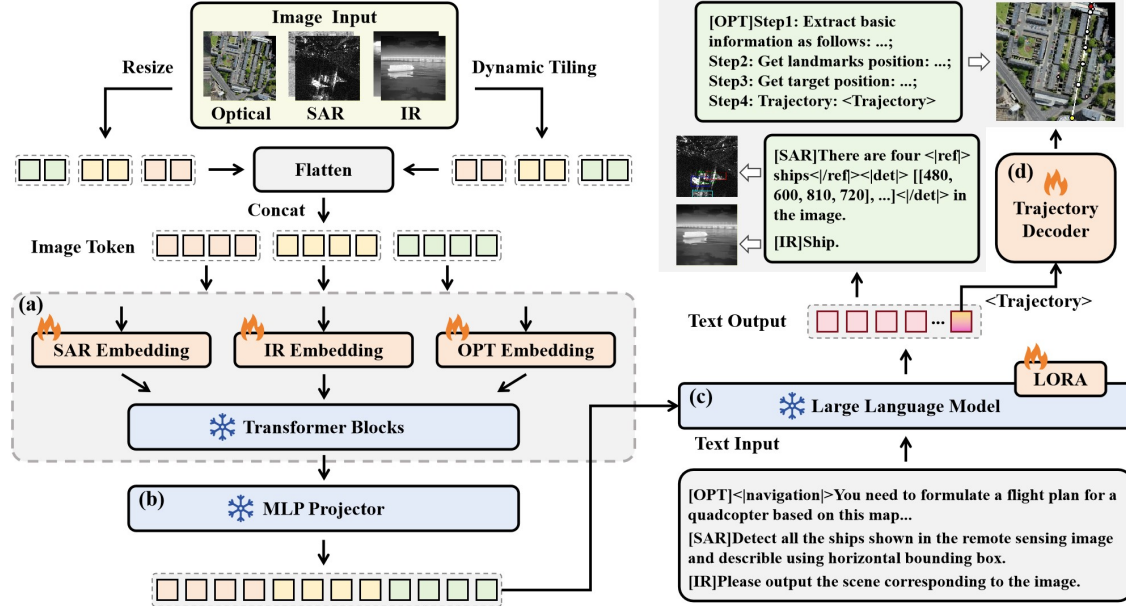


Figure 4: The overall architecture of RingMo-Agent, which supports image inputs from multiple platforms and modalities, enabling both perception and reasoning capabilities. The image features are fed into (a) a visual encoder. After passing through (b) a frozen MLP and (c) a LLM fine-tuned via LoRA, the model directly generates textual content, with (d) additional decoding applied for tasks involving trajectory outputs.

4.1 Architecture

The proposed RingMo-Agent comprises four main components: a visual encoder for extracting visual features, a LLM for processing language information, an MLP projector serving as an intermediate adapter that projects visual features into the semantic space of the language model, and a trajectory decoder designed for spatiotemporal modeling, as illustrated in Figure 4. Our approach employs a two-stage training strategy that unifies multi-source data such as optical, infrared, and SAR imagery, while also extending conventional perception tasks to more challenging reasoning tasks, such as complex urban scene understanding from UAV perspectives.

Visual Encoder. The visual encoder is based on the SigLIP [73] method, dynamically rescaling input images to multiples of 384 while accommodating RS images with varying aspect ratios. In particular, given an input image of size $(H \times W \times C) \in \mathbb{R}$, the image is rescaled to dimensions $m \times 384, n \times 384, c$, where $m, n \in \mathbb{N}, 1 \leq m, n, mn \leq 9$. The values of m and n are determined by selecting the smallest multiples of 384 that are greater than or equal to the original image height H and width W , respectively. Following this resizing step, the image is partitioned into independent patches of size 384×384 . Additionally, a global thumbnail is generated by directly resizing the image to 384×384 to provide a coarse global representation.

Most existing research focuses on single-modality optical learning, while distribution gaps across modalities limit the effectiveness of a unified encoder. To address this issue, we adopt modality-specific embedding layers for optical, SAR, and infrared inputs. Specifically, three parallel patch embedding layers with shared architecture but independent

Algorithm 1 Trajectory Decoding from Predicted Tokens

Input: The hidden representation of the `< trajectory >` token h_{tra} , the global visual embedding v , the goal embedding g , the previous-point embedding b , maximum termination step T , termination threshold p , finished flag P_{flag} .

Output: Updated trajectory S .

```

1:  $h_0 \leftarrow \text{LatentProjection}(h_{tra})$ 
2: while  $t \leq T \text{ && } P_{flag}$  do:
3:    $f_t \leftarrow \text{Concatenate}(h_0, v, g, b)$ 
4:    $h_t \leftarrow \text{GRUCell}(f_t, h_{t-1})$ 
5:    $S_t \leftarrow \text{OutputProjection}(h_t)$ 
6:    $S \leftarrow \text{Update}(S_t)$ 
7:    $P_{flag} \leftarrow \text{TerminationCondition}(S_t, p)$ 
8:    $t \leftarrow t + 1$ 
9: end while

```

parameters are used to project each modality into a unified 1152-dimensional embedding space, thereby reducing cross-modal interference. To formalize this process, let $x_{\text{opt}}, x_{\text{ir}}, x_{\text{sar}} \in \mathbb{R}^{H \times W \times C}$ represent the input images from the optical, infrared, and SAR modalities, respectively. The visual embeddings for each modality are obtained as:

$$z_{\text{opt}} = E_{\text{opt}}(x_{\text{opt}}), \quad z_{\text{ir}} = E_{\text{ir}}(x_{\text{ir}}), \quad z_{\text{sar}} = E_{\text{sar}}(x_{\text{sar}}), \quad (1)$$

where E_{opt} , E_{ir} , and E_{sar} are the embedding layers for optical, infrared, and SAR data, respectively. These embeddings are then forwarded to the subsequent image encoder for further processing. The frozen visual encoder, denoted as F_V , receives an input image z and outputs the corresponding visual features:

$$V = F_V(z), \quad z = \{z_{\text{opt}}, z_{\text{ir}}, z_{\text{sar}}\}, \quad (2)$$

where V represents the extracted visual features.

Frozen MLP Projector. The adapter follows an MLP architecture composed of linear layers. Following the setup of DeepSeek-VL2 [40], the mapping performed by the adapter can be represented by the following computation:

$$Q = F_A(V), \quad (3)$$

where, F_A denotes the adapter composed of MLP layers, and Q represents the mapped features. In F_A , a 2×2 shuffling operation is first applied to transform each tile's visual tokens from a 27×27 layout to 14×14 . Subsequently, three types of special tokens are inserted into the visual features to serve as positional indicators: one is appended to the end of each row in the global thumbnail tile, another to the end of the last column in the local tiles, and the third is placed between the global and local tiles. Then, as illustrated in Figure 4, the processed embeddings are fed into the LLM as input.

LoRA-Fine-Tuned Large Language Model. The LLM is built on the DeepSeekMoE architecture [5, 6], which introduces multi-head latent attention by compressing the Key-Value cache into a latent representation to reduce training costs. We use the 3B variant of DeepSeek-VL2 [40] and apply LoRA [74] for parameter-efficient adaptation by inserting a small number of trainable low-rank matrices into the query and value projection layers of the LLM self-attention block, with a rank of 64 and a scaling factor of 16. Fine-tuning is then performed only on these additional parameters. The process can be formulated as follows:

$$\hat{y} = F_L(Q, x_{\text{txt}}), \quad (4)$$

where, F_L denotes the LLM fine-tuned with LoRA, x_{txt} represents the textual input, and \hat{y} represents the output results.

Trainable Trajectory Decoder. Conventional models generate text or 2D coordinates via sequential token decoding, limiting spatial motion modeling. Inspired by LISA [30], we propose a high-dimensional hidden state decoding mechanism using task-specific tokens to explicitly capture dynamic trajectories from the final transformer layer. By jointly integrating global image features and other embedding vectors, this mechanism improves temporal action continuity. The detailed procedure of the decoding mechanism is described in Algorithm 1. The special token `< trajectory >` is predicted only in the task scheduling scenario, where coordinate outputs are required, enabling end-to-end training within a unified framework.

Specifically, let h_{tra} denote the embedding vector of the `< trajectory >` token in the last layer. We define the internal computations of the trajectory decoder as follows:

$$h_0 = \phi_{\text{latent}}(h_{\text{tra}}), \quad (5)$$

where ϕ_{latent} is a linear projection. The latent vector is projected into the hidden state space to obtain the initial hidden state h_0 , encoding the contextual features of the current environment. At each time step t , the decoder updates the hidden state and predicts the next trajectory state as:

$$h_t = \text{GRUCell}(f_t, h_{t-1}), \quad (6)$$

where h_t represents the updated hidden state, and f_t is constructed by concatenating the 256-dimensional embeddings of the previous point, the global visual feature, the goal location, and the initial hidden state h_0 , all of which are obtained via linear projections.

Then, the next trajectory state is predicted from the hidden state via an output projection layer:

$$S_t = \phi_{\text{output}}(h_t), \quad (7)$$

where ϕ_{output} is a linear projection that predicts the offset of the next point. The predicted trajectory state at each step is appended to the corresponding trajectory sequence S . We set the termination distance threshold to 1e-3, and define the maximum number of steps based on the longest trajectory in the scenario. The loop terminates when either condition is met.

The constraint loss consists of two components: a cross-entropy loss L_{txt} for text prediction, and a mean squared error loss L_{mse} applied to each trajectory point for trajectory regression. The overall objective is their weighted sum:

$$L = \lambda_{\text{txt}} L_{\text{txt}} + \lambda_{\text{mse}} L_{\text{mse}}, \quad (8)$$

where the coefficients are set to $\lambda_{\text{txt}} = 1$ and $\lambda_{\text{mse}} = 5$.

4.2 Training Methodology

RingMo-Agent employs a two-stage training approach, consisting of the vision-language generation stage and the instruction-tuning stage.

In the vision-language generation stage, the primary objective is to adapt the model from natural scene understanding to the RS image domain. The original pretrained weights struggle to handle complex RS scenes, often misidentifying multiple distinct objects as a single entity, making it insufficient for fine-grained recognition tasks. To address this issue, we utilize paired RS image-text data for generative training. In this process, we adopt image-text paired datasets to enable optimization via the generative loss of LLMs. The data is sourced from publicly available classification, captioning, and detection datasets [53, 54, 60, 61, 63–65, 75–79]. For all datasets involved in the experiments of this paper, we use only the training split. To enhance linguistic diversity while preserving semantic accuracy, we use GPT-4 [9] to expand the original annotations, applying constraints such as requiring the generated sentence to contain the original ground truth. Additionally, we employ rule-based extraction methods to verify whether the generated descriptions accurately reflect the original labels. In the instruction-tuning stage, the model is optimized to generate outputs that align with the given instructions, ensuring accurate task execution.

5 Experiments

This section details the training procedure and evaluates the instruction-tuned model on both perception tasks (detection, VQA, classification, captioning) and reasoning tasks (relation reasoning, task scheduling, instruction decomposition, action decision), using both qualitative and quantitative analyses.

In the reported results, FT denotes the fine-tuned results, while ZS refers to the zero-shot results. **Bold** indicates the best performance, and underline denotes the second-best.

5.1 Experimental Settings

During vision-language generation stage, we train our model on 8 NVIDIA A100 GPUs (80 GB) using the AdamW optimizer. The learning rate follows a linear warmup followed by a cosine decay schedule, with an initial learning rate of 1e-4, a warmup learning rate of 1e-6, and a minimum learning rate of 1e-5. We apply a weight decay of 0.05 for regularization and train the model on over 500,000 samples for 10 epochs, with the image size fixed at 384.

During instruction-tuning stage, RingMo-Agent adopts a linear warmup followed by a cosine decay learning rate schedule. The training utilizes the AdamW optimizer, with an initial learning rate of 1e-6, a warmup starting from 1e-8, and a minimum learning rate decaying to 0. To further enhance generalization and mitigate overfitting, a weight decay of 0.05 is applied throughout the optimization process. In this stage, we impose no restriction on image resolution and retain the original dimensions of each sample. The model is also trained for 10 epochs. The combined training, validation, and test sets contain over 3 million samples, collectively referred to as RS-VL3M. For the evaluation datasets used to report accuracy, we conduct separate fine-tuning in addition to the zero-shot setting.

5.2 Task Scheduling

Dataset. We use the CityNav dataset [57], which comprises 34 diverse urban scene environments. The dataset encompasses a wide range of target object categories.

Metrics. We evaluate on all three test splits. Following CityNav [57], four metrics are used to assess the accuracy of the generated trajectories: Navigation Error (NE), Success Rate (SR), Oracle Success Rate (OSR), and Success weighted by Path Length (SPL).

Table 3: Evaluation results on the CityNav dataset.

Model	Validation Seen				Validation Unseen				Test Unseen			
	NE ↓	SR ↑	OSR ↑	SPL ↑	NE ↓	SR ↑	OSR ↑	SPL ↑	NE ↓	SR ↑	OSR ↑	SPL ↑
Specialist models												
Seq2Seq (FT) [80]	257.1	1.81	7.89	1.58	317.4	0.79	8.82	0.61	245.3	1.50	8.34	1.30
CMA (FT) [81]	240.8	0.95	9.42	0.92	268.8	0.65	7.86	0.63	252.6	0.82	9.70	0.79
AerialVLN + GSM (FT) [57]	56.6	10.16	22.20	7.89	72.7	6.35	15.24	5.06	85.1	6.72	18.21	5.16
RSVLMs												
RingMo-Agent (FT)	<u>132.0</u>	<u>5.89</u>	<u>21.39</u>	<u>5.24</u>	<u>156.0</u>	<u>4.91</u>	<u>17.22</u>	<u>4.33</u>	<u>149.6</u>	<u>4.74</u>	<u>18.94</u>	<u>4.17</u>

Results. As shown in Table 3, RingMo-Agent outperforms the fine-tuned Seq2Seq [80] and CMA [81], and approaches the performance of AerialVLN [57], which incorporates map encoding and multi-view features. Unlike AerialVLN, we achieve competitive results without relying on external map priors, with only a 1.44% SR gap on the unseen validation set. Current general-purpose vision-language models (VLMs) and remote sensing vision-language models (RSVLMs) still struggle to complete this complex spatial navigation task.

5.3 Action Decision

Dataset. We evaluate this task on the SkyAgent-Plan3k [50] dataset, which encompasses four distinct urban scene types: Shanghai, Shenzhen, Campus, and Residence.

Metrics. To assess the quality of the generated step-by-step action plans, we adopt BLEU and SPICE as evaluation metrics.

Table 4: Evaluation results on the SkyAgent-Plan3k dataset.

Model	ShangHai		ShenZhen		Campus		Residence	
	BLEU-1 ↑	SPICE ↑						
VLMs								
InstructBLIP-Flan-T5-XXL (ZS) [26]	0.04	5.79	0.03	4.23	0.95	4.58	0.14	7.20
InstructBLIP-Vicuna-7B (ZS) [26]	0.15	0.68	0.04	3.23	0.74	1.21	0.18	1.86
InstructBLIP-Vicuna-13B (ZS) [26]	0.12	1.14	0.34	2.18	0.63	0.46	0.07	1.51
MiniGPT-4 (ZS) [82]	12.88	4.03	13.96	4.51	16.89	4.25	15.85	4.51
GPT-4o (ZS) [34]	10.64	5.12	11.52	5.20	11.67	5.03	11.83	4.83
Qwen-VL (ZS) [36]	15.74	5.41	15.36	5.06	12.18	3.10	10.01	3.75
RSVLMs								
SkyAgent (FT) [50]	40.87	<u>26.53</u>	<u>36.05</u>	<u>24.04</u>	<u>34.03</u>	<u>22.57</u>	<u>42.56</u>	<u>24.29</u>
RingMo-Agent (FT)	<u>37.33</u>	31.68	37.76	31.85	42.79	28.45	42.78	37.68

Results. As shown in Table 4, our method demonstrates clear advantages over the baseline approaches across all scene categories. Existing RSVLMs have yet to explore their reasoning capabilities in 3D space guided by multi-image inputs. These results validate the effectiveness of our model in bridging the gap between visual-language reasoning and actionable control.

5.4 Relation Reasoning

Dataset. We conduct evaluation experiments on two relation reasoning datasets: the FIT-RS dataset [19] and our self-constructed ReCon1M-REL dataset. The FIT-RS dataset includes 54 relation categories, with all images cropped to a fixed resolution of 512×512 . In contrast, ReCon1M-REL retains 59 relation categories and adopts variable resolutions.

Metrics. We use F1-score to assess this task.

Table 5: Evaluation results on the FIT-RS and ReCon1M-REL datasets.

Model	FIT-RS	ReCon1M-REL
	F1-score ↑	F1-score ↑
VLMs		
MiniGPT-v2 (ZS) [27]	0.00	0.00
DeepSeek-VL2 (ZS) [40]	0.06	0.30
Kosmos-2 (ZS) [28]	0.00	0.15
Shikra (ZS) [29]	0.52	0.65
Qwen3-VL (ZS) [38]	0.00	<u>4.56</u>
Gemini 2.5 (ZS) [33]	0.41	1.36
GPT-4o (ZS) [34]	3.32	3.04
RSVLMs		
SkySenseGPT (FT) [19]	<u>74.33</u>	-
RingMo-Agent (FT)	75.34	90.23

Results. As presented in Table 5, RingMo-Agent demonstrates superior performance, achieving an accuracy of 75.34%, which slightly surpasses the 74.33% obtained by SkySenseGPT [19]. On ReCon1M-REL dataset, we achieve the F1-score of 90.23%. In contrast, state-of-the-art VLMs [33, 34, 38] are still unable to effectively perform such tasks, even when provided with more explicit prompts. This limitation primarily stems from the lack of targeted training that emphasizes relation reasoning among objects in wide-field images, which consequently leads to substantially degraded performance.

5.5 Instruction Decomposition

Dataset. We evaluate our model on the self-constructed ReCon1M-DEC dataset.

Metrics. To comprehensively assess performance, we evaluate the models using mAP@50, which measures mean Average Precision at an Intersection-over-Union threshold of 0.5, and the F1-score.

Table 6: Evaluation results on the ReCon1M-DEC dataset.

Model	mAP@50 ↑	F1-Score ↑
VLMs		
MiniGPT-v2 (ZS) [27]	0.00	0.00
DeepSeek-VL2 (ZS) [40]	0.00	0.00
Qwen3-VL (ZS) [38]	0.28	0.03
Gemini 2.5 (ZS) [33]	<u>0.50</u>	0.07
GPT-4o (ZS) [34]	0.14	<u>0.13</u>
RSVLMs		
RingMo-Agent (FT)	24.20	32.85

Results. Table 6 reports object recognition accuracy and relation reasoning performance within the target region. We employ carefully designed prompts to evaluate advanced VLMs as baselines. As shown, existing VLMs exhibit notably low accuracy, largely due to insufficient training emphasis on object categories, spatial locations, and inter-object relationships in wide-area scenes. Consequently, when multiple objects are present, these models typically predict only one or two instances, failing to reflect the true object multiplicity. In contrast, RingMo-Agent effectively handles the challenging ReCon1M-DEC dataset by capturing fine-grained features of small objects and producing correct one-to-one relational predictions, achieving an mAP@50 of 24.20% for object detection and an F1-score of 32.85% for intra-region relation detection.

5.6 Image Captioning

Dataset. We conduct evaluation separately on optical, SAR, and infrared modalities. The optical datasets utilize UCM-Captions [60] and NWPU-Captions [62], while the SAR and infrared modalities are tested on our self-constructed datasets.

Metrics. The performance is reported using BLEU, METEOR, ROUGE-L, and CIDEr metrics.

Table 7: Evaluation results on the SAR-CAP and IR-CAP datasets.

Model	SAR-CAP						IR-CAP					
	BLEU-1 ↑	BLEU-2 ↑	BLEU-3 ↑	BLEU-4 ↑	METEOR ↑	ROUGE-L ↑	BLEU-1 ↑	BLEU-2 ↑	BLEU-3 ↑	BLEU-4 ↑	METEOR ↑	ROUGE-L ↑
VLMs												
MiniGPT-v2 (ZS) [27]	7.00	3.64	1.59	0.60	7.67	9.25	5.65	3.35	1.92	0.98	7.62	8.67
DeepSeek-VL2 (ZS) [40]	12.52	5.88	1.88	0.60	10.65	14.10	13.95	7.57	3.47	1.43	12.48	15.12
Qwen3-VL (ZS) [38]	12.51	5.70	1.43	0.42	11.74	12.85	7.62	4.30	1.91	0.82	8.43	9.90
Gemini 2.5 (ZS) [33]	13.00	5.43	1.81	0.77	12.46	13.23	17.70	7.76	3.17	1.32	14.14	17.99
GPT-4o (ZS) [34]	19.93	9.76	3.14	1.15	13.52	19.24	28.05	14.43	6.15	2.41	16.23	26.76
RSVLMs												
RingMo-Agent (FT)	55.93	44.49	33.57	23.94	25.06	51.12	56.84	40.45	29.17	21.50	26.15	43.13

Table 8: Evaluation results on the UCM Dataset.

Model	BLEU-4 ↑	METEOR ↑	ROUGE-L ↑	CIDEr ↑
Specialist models				
SAA (FT) [83]	64.77	38.59	69.42	294.51
Post-processing (FT) [84]	62.62	40.80	74.06	309.64
VLMs				
MiniGPT-4 (ZS) [82]	18.10	33.36	41.37	0.03
Shikra (ZS) [29]	33.98	32.56	56.73	56.69
MiniGPT-v2 (ZS) [27]	36.16	32.41	56.57	60.66
DeepSeek-VL2 (ZS) [40]	5.44	15.95	27.22	26.42
Qwen3-VL (ZS) [38]	1.82	15.73	24.92	8.85
Gemini 2.5 (ZS) [33]	2.78	17.05	25.96	11.74
GPT-4o (ZS) [34]	3.33	15.37	26.31	21.13
RSVLMs				
RSGPT (FT) [23]	65.74	42.21	78.34	333.23
RingMoGPT (FT) [22]	-	49.90	83.29	359.32
RS-CapRet (FT) [16]	67.00	47.20	81.70	354.80
RS-LLaVA (FT) [24]	72.84	47.98	85.17	349.43
SkyEyeGPT (FT) [18]	78.41	46.24	79.49	236.75
RingMo-Agent (FT)	77.63	51.79	85.51	373.68

Table 9: Zero-shot results on the NWPU-Captions dataset.

Model	METEOR ↑	ROUGE-L ↑	CIDEr ↑
VLMs			
Qwen-VL [36]	12.60	26.24	24.64
MiniGPT-v2 [27]	13.70	26.60	19.70
LLaVA [85]	13.70	28.80	32.60
DeepSeek-VL2 [40]	14.88	19.56	3.18
Qwen3-VL [38]	15.92	23.91	7.72
Gemini 2.5 [33]	16.17	24.00	8.40
GPT-4o [34]	15.93	27.33	15.33
RSVLMs			
RingMoGPT [22]	20.90	37.50	74.70
RingMo-Agent	<u>18.81</u>	<u>34.11</u>	<u>48.39</u>

Results. As shown in Table 8 and Table 9, RingMo-Agent consistently outperforms both specialized models and VLMs on the UCM-Captions [60] and NWPU-Captions [62] optical image captioning datasets. On UCM-Captions, it achieves a METEOR score of 51.79, a ROUGE-L score of 85.51, and a CIDEr score of 373.68, surpassing existing RSVLMs. Furthermore, on SAR and infrared captioning benchmarks (Table 7), RingMo-Agent demonstrates a clear advantage over advanced VLMs such as Qwen3-VL [38]. This performance gap arises because these models are insufficiently trained on multi-modal RS data; in particular, on SAR imagery, they tend to misclassify objects such as ships and aircraft as stars.

5.7 VQA

Dataset. We report the fine-tuned result on RSVQA-LR [51] test set and zero-shot result on RSVQA-HR [51]. These benchmarks assess the model’s ability to understand object types, quantities, and spatial locations.

Metrics. We compute the accuracy for each question type as well as the overall average accuracy.

Table 10: Evaluation results on the RSVQA-LR Dataset.

Model	Pre. Acc \uparrow	Comp. Acc \uparrow	Avg. Acc \uparrow
Specialist models			
EasyToHard (FT) [86]	90.66	87.49	89.08
Bi-Modal (FT) [87]	91.06	91.16	91.11
SHRNet (FT) [88]	91.03	90.48	90.76
VLMs			
MiniGPT-4 (ZS) [82]	43.86	57.55	50.71
Shikra (ZS) [29]	46.47	60.31	53.39
Qwen-VL (ZS) [36]	38.57	67.59	53.08
MiniGPT-v2 (ZS) [27]	49.85	63.09	56.47
InstructBLIP (ZS) [26]	48.83	65.92	57.38
mPLUG-Owl2 (ZS) [89]	74.04	63.69	68.87
LLaVA-1.5 (ZS) [90]	55.46	68.20	61.83
DeepSeek-VL2 (ZS) [40]	55.33	66.87	61.10
Qwen3-VL (ZS) [38]	66.53	77.49	72.01
Gemini 2.5 (ZS) [33]	67.99	72.77	70.38
GPT-4o (ZS) [34]	69.20	63.14	66.17
RSVLMs			
RSGPT (FT) [23]	91.17	91.70	91.44
Geochat (FT) [20]	91.09	90.33	90.71
LHRS-Bot (FT) [17]	89.07	88.51	88.79
H ² RSVLM (FT) [21]	89.58	89.79	89.69
RS-LLaVA (FT) [24]	92.80	91.33	92.07
SkyEyeGPT (FT) [18]	88.93	88.63	88.78
RingMo-Agent (FT)	93.10	87.50	90.30

Table 11: Zero-shot results on the RSVQA-HR dataset.

Model	Pre. Acc \uparrow	Comp. Acc \uparrow	Avg. Acc \uparrow
VLMs			
Qwen-VL (ZS) [36]	66.44	60.41	63.43
LLaVA-v1.5 [85]	69.83	67.29	68.56
MiniGPT-v2 [27]	40.79	50.91	45.85
RSVLMs			
EarthGPT [14]	62.77	79.53	71.15
Geochat [20]	58.45	83.19	70.82
H ² RSVLM [21]	65.00	83.70	74.35
SkySenseGPT [19]	69.14	84.14	76.64
RingMo-Agent	75.24	83.92	79.58

Results. Table 10 presents the results on RSVQA-LR, focusing on two question types: Presence and Comparison. Compared with other methods, we achieve 93.10% accuracy on presence questions, surpassing RS-LLaVA [24] by 0.3%. Table 11 shows that we achieve accuracies of 75.24% on presence questions, 83.92% on comparison questions, and an overall average accuracy of 79.58%. Moreover, our model consistently outperforms VLMs on both datasets, further demonstrating its suitability for RS applications.

5.8 Classification

Dataset. We report results on the AID [52] and NWPU-RESISC45 [63] datasets, along with our self-constructed IR-CLA and SAR-CLA datasets, and provide zero-shot results on UCMerced-LandUse [65] and WHU-RS19 [64].

Metrics. For optical datasets, following the approach of GeoChat [20], we use all categories as candidate answers to prevent synonymous outputs. For infrared and SAR datasets, all categories are provided as candidate answers for VLMs.

Results. As shown in Table 12, RingMo-Agent achieves strong performance on optical tasks, reaching 93.96% accuracy on NWPU-RESISC45. On the zero-shot set UCMerced-LandUse, we achieve 86.52%, surpassing other RSVLMs, as shown in Table 13. This improvement is attributed to the robust generalization ability of the model.

Table 12: Evaluation results on the AID and NWPU-RESISC45 datasets.

Model	AID (Acc \uparrow)	NWPU-RESISC45 (Acc \uparrow)
Specialist models		
LSENet (FT) [91]	94.41	93.34
SeCo-ResNet-50 (FT) [92]	<u>93.47</u>	92.91
VLMs		
MiniGPT-4 (ZS) [82]	43.86	57.55
DeepSeek-VL2 (ZS) [40]	35.63	17.60
Qwen3-VL (ZS) [38]	70.71	71.01
Gemini 2.5 (ZS) [33]	37.97	68.58
GPT-4o (ZS) [34]	58.33	50.52
RSVLMs		
EarthGPT (FT) [14]	-	<u>93.84</u>
RingMo-Agent (FT)	92.43	93.96

Table 13: Zero-shot results on the WHU-RS19 and UCMerced-LandUse datasets.

Model	WHU-RS19 (Acc \uparrow)	UCMerced-LandUse (Acc \uparrow)
VLMs		
Qwen-VL [36]	83.51	62.90
MiniGPT-v2 [27]	62.08	4.76
LLaVA [85]	74.52	68.00
CLIP [93]	87.50	-
DeepSeek-VL2 [40]	69.05	32.00
Qwen3-VL [38]	82.39	77.81
Gemini 2.5 [33]	47.56	65.10
GPT-4o [34]	85.27	43.52
RSVLMs		
RemoteCLIP [49]	94.66	-
GeoChat [20]	86.47	84.43
RingMoGPT [22]	97.71	<u>86.48</u>
SkySenseGPT [19]	<u>97.02</u>	-
RingMo-Agent	95.28	86.52

Table 14: Evaluation results on the SAR-CLA and IR-CLA datasets.

Model	SAR-CLA	IR-CLA
	Acc \uparrow	Acc \uparrow
VLMs		
DeepSeek-VL2 (ZS) [40]	5.22	95.56
Qwen3-VL (ZS) [38]	29.38	98.21
Gemini 2.5 (ZS) [33]	<u>37.89</u>	97.55
GPT-4o (ZS) [34]	36.74	<u>98.42</u>
RSVLMs		
RingMo-Agent (FT)	92.67	99.45

5.9 Object Detection

Dataset. RingMo-Agent supports object detection across three modalities: optical, SAR, and infrared. SAR results are reported on SARDet-100k [59], and infrared results on our IR-DET dataset.

Metrics. We report both per-class and overall detection performance using mAP@50.

Results. As shown in Table 16 and Table 15, RingMo-Agent significantly outperforms existing models in SAR and infrared object detection. Although advanced generalist VLMs are used as baselines and demonstrate strong detection ability on natural images, they struggle with specific modalities in RS. For instance, Qwen3-VL [38] often misinterprets SAR images as dark or gray sky scenes, reflecting a misunderstanding of SAR imaging characteristics. On the IR-DET dataset, these models can partially recognize common objects such as vehicles and trucks, yet achieve near-zero performance on most categories. This degradation mainly results from the severe modality shift between natural RGB imagery and non-optical remote sensing data, such as SAR and infrared images, whose physical imaging mechanisms and visual patterns fundamentally differ from those seen during VLM pre-training.

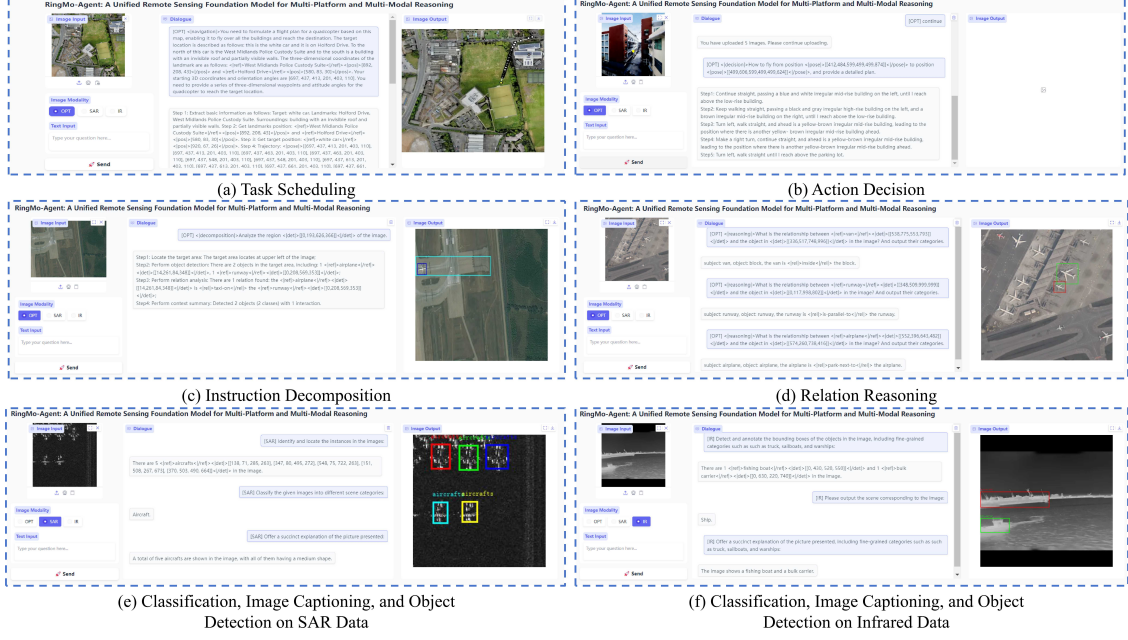


Figure 5: The visual results presented by RingMo-Agent in response to user questions about image content.

Table 15: Evaluation results on the IR-DET dataset.

Model	Fine-Grained Categories													Coarse-Grained Categories				mAP@50↑
	Bulk Carrier	Bus	Canoe	Container Ship	Fishing Boat	Liner	Nonmotor Vehicle	Other Vehicle	Sailboat	Truck	Warship	Bike	Cyclist	People	Ship	Vehicle		
VLMs																		
MiniGPT-v2 (ZS) [27]	0.00	0.00	0.00	0.00	0.00	0.00	0.00	0.00	0.00	0.00	0.00	0.00	0.00	0.00	0.00	0.00	0.00	
DeepSeek-VL2 (ZS) [40]	0.00	0.00	0.00	0.00	0.00	0.00	0.00	0.00	0.00	0.00	0.00	0.00	0.00	0.00	0.00	0.00	0.00	
Kosmos-2 (ZS) [28]	0.00	8.75	0.00	0.00	0.00	0.00	0.00	0.00	3.96	1.78	0.00	0.00	0.00	1.23	2.13	7.76	1.60	
shikra (ZS) [29]	0.00	1.81	0.00	0.00	0.00	0.00	0.31	0.00	0.91	0.52	0.00	0.00	0.95	0.28	0.73	0.34		
Qwen3-VL (ZS) [38]	0.00	13.34	0.00	0.00	0.00	0.90	0.15	0.00	8.85	16.06	13.01	0.00	0.00	1.35	6.17	19.11	4.93	
Gemini 2.5 (ZS) [33]	0.00	28.79	0.00	0.00	0.00	1.18	0.14	0.00	2.18	13.95	24.82	0.00	0.50	8.26	2.27	22.70	6.55	
GPT-4o (ZS) [34]	0.00	0.25	0.00	0.00	0.00	0.00	0.00	0.00	0.02	0.02	0.00	0.00	0.00	0.00	0.00	0.03	0.02	
RSVLMs																		
RingMo-Agent (FT)	70.63	21.25	74.43	59.77	91.47	87.03	78.11	62.71	70.80	39.61	89.66	35.95	16.61	53.67	42.52	63.83	59.88	

Table 16: Evaluation results on the SARDet-100k dataset.

Model	Ship	Aircraft	Bridge	Harbor	Car	Tank	mAP@50↑
VLMs							
MiniGPT-v2 (ZS) [27]	0.00	0.00	0.00	0.00	0.00	0.00	0.00
DeepSeek-VL2 (ZS) [40]	0.00	0.00	0.00	0.00	0.00	0.00	0.00
Kosmos-2 (ZS) [28]	0.27	0.17	0.00	0.00	0.04	0.00	0.08
shikra (ZS) [29]	0.00	0.00	0.00	0.00	0.00	0.00	0.00
Qwen3-VL (ZS) [38]	0.89	0.09	0.00	0.00	0.33	0.00	0.22
Gemini 2.5 (ZS) [33]	1.46	0.14	0.00	0.00	0.00	0.00	0.27
GPT-4o (ZS) [34]	0.03	0.00	0.00	0.00	0.00	0.00	0.01
RSVLMs							
RingMo-Agent (FT)	74.43	52.93	49.90	62.30	63.37	20.10	53.84

5.10 Ablation Study

To assess the effectiveness of key design components within RingMo-Agent, we conduct ablation experiments from three perspectives: (1) the impact of the two-stage training paradigm, (2) the role of modality-specific embedding layers, and (3) the function of the trajectory decoder.

Two-Stage Training. We pretrain RingMo-Agent on a large-scale RS image-text dataset to enhance image-text generation. To assess the impact, we compare it with a baseline initialized from DeepSeek-VL2 without pretraining, using identical datasets and training strategies. As shown in Table 17 and Table 18, the two-stage training consistently improves performance on both reasoning and perception tasks. This gain stems from the ability to capture RS-specific features such as resolution, viewpoint, and spectral differences, thereby boosting generalization.

Modality-Specific Embedding Layers. We fine-tune separate embedding layers for optical, SAR, and infrared modalities, guided by modality labels during training and inference. Only the embedding layers are updated, while the rest of the visual encoder remains frozen. As shown in Table 19, freezing these layers and removing modality-specific

Table 17: Ablation results on the impact of two-stage training for reasoning tasks.

Model	Relation Reasoning		Instruction Decomposition	
	FIT-RS (F1-score \uparrow)	ReCon1M-REL (F1-score \uparrow)	ReCon1M-DEC (mAP@50 \uparrow)	ReCon1M-DEC (F1-score \uparrow)
RingMo-Agent (one stage)	72.82	87.11	16.72	20.32
RingMo-Agent (two stage)	75.34	90.23	24.20	32.85

Table 18: Ablation results on the impact of two-stage training for perception tasks.

Model	Object Detection			Image Captioning			VQA	
	SARDet-100k (mAP@50 \uparrow)	IR-DET (mAP@50 \uparrow)	UCM (BLEU-4 \uparrow)	SAR-CAP (BLEU-1 \uparrow)	IR-CAP (BLEU-1 \uparrow)	RSVQA-LR (Avg. Acc \uparrow)		
RingMo-Agent (one stage)	50.12	51.56	76.12	50.12	49.16	89.96		
RingMo-Agent (two stage)	53.84	59.88	77.63	55.93	56.84	90.30		

Table 19: Ablation results on the impact of modality-specific embedding layers, where MSEL denotes modality-specific embedding layers.

Model	MSEL	Object Detection			Image Captioning			Image Classification		
		SARDet-100k (mAP@50 \uparrow)	IR-DET (mAP@50 \uparrow)	UCM (BLEU-4 \uparrow)	SAR-CAP (BLEU-1 \uparrow)	IR-CAP (BLEU-1 \uparrow)	SAR-CLA (Acc \uparrow)	IR-CLA (Acc \uparrow)		
RingMo-Agent	✗	48.10	51.23	74.11	46.32	51.08	88.17	96.60		
RingMo-Agent	✓	53.84	59.88	77.63	55.93	56.84	92.67	99.45		

Table 20: Ablation results on the impact of trajectory decoder.

Model	Trajectory Decoder	Validation Seen				Validation Unseen				Test Unseen			
		NE \downarrow	SR \uparrow	OSR \uparrow	SPL \uparrow	NE \downarrow	SR \uparrow	OSR \uparrow	SPL \uparrow	NE \downarrow	SR \uparrow	OSR \uparrow	SPL \uparrow
RingMo-Agent	✗	196.4	2.65	14.23	2.16	220.1	1.94	12.36	1.91	187.9	1.57	13.16	1.22
RingMo-Agent	✓	132.0	5.89	21.39	5.24	156.0	4.91	17.22	4.33	149.6	4.74	18.94	4.17

design degrades performance, highlighting the importance of dedicated extractors. Despite sharing identical structures, separate embeddings better capture modality-specific characteristics, avoiding feature degradation caused by forcing heterogeneous data through shared filters.

Trajectory Decoder. To address challenges such as loss imbalance and difficulty in sequential constraints when LLMs generate point-by-point trajectories, we additionally designed a trajectory decoder specifically for task scheduling. In Table 20, we additionally compare the case without using the trajectory decoder, where the model predicts the next token sequentially to output the six-dimensional coordinates for each point. The results on the CityNav dataset [57] demonstrate the effectiveness of the trajectory decoder, showing improved performance in both seen and unseen scenarios.

5.11 Visualization

To provide a clearer understanding of the model behavior, we present visualizations of representative results in this work, as shown in Figure 5. These include task scheduling (a), action decision (b), instruction decomposition (c), relation reasoning (d), as well as classification, captioning, and detection on SAR and infrared data (e, f). Additionally, Figure 6 provides visualized examples to demonstrate the dialogue interactions.

6 Conclusion

In this work, we propose RingMo-Agent, a unified foundation model tailored for RS data across multiple platforms and modalities. It is capable of handling images with diverse viewing angles and sensing characteristics, and performing complex reasoning tasks. The model benefits from several key supports: a large-scale dataset RS-VL3M comprising over 3 million image-text pairs; the construction of separated embedding layers to address distribution differences across modalities and isolate the feature extraction process; and the introduction of a token-based high-dimensional hidden state decoding mechanism for long-horizon spatial tasks, which significantly expands the task coverage. We envision that future RS agents will further advance toward deeper logical reasoning abilities, thereby supporting real-world applications such as damage assessment and decision-making in emergency scenarios like disaster response.

Examples			
Image	Task	Question	Answer
	Image Captioning	[SAR] Offer a succinct explanation of the picture presented:	This image shows five aircrafts on a runway.
	Image Classification	[IR] What is the scene category of the given image:	Ship.
	Object Detection	[OPT] Detect and annotate the bounding boxes of the objects in the image:	There are 4 <ref>aircrafts</ref><det>[[107, 149, 384, 533], [117, 544, 428, 922], [680, 213, 964, 604], [698, 615, 985, 989]]</det> in the image.
	Visual Question Answer	[OPT] Question how can people improve their strength in this image? short answer:	Aerobic.
	Relation Reasoning	[OPT] <reasoning>What is the relationship between <ref>solar-panel</ref><det>[[170,546,242,646]]</det> and the object in <det>[[0,236,301,872]]</det> in the image? And output their categories.	Subject: solar panel, object: building, the solar-panel is <ref>power</ref> the building.
	Instruction Decomposition	[OPT] <decomposition>Break down visual elements in region <det>[[343,641,586,739]]</det>.	Step1: Locate the target area: The target area locates at lower area of the image. Step2: Perform object detection: There are 2 objects in the target area, including: 2 <ref>airplanes</ref><det>[[365,651,446,732], [490,649,566,731]]</det>. Step3: Perform relation analysis: There are 2 relations found: the <ref>airplane</ref><det>[[490,649,566,731]]</det> is <ref>park-next-to</ref> the <ref>airplane</ref><det>[[365,651,446,732]]</det>... Step4: Perform context summary: Detected 2 objects (1 class) with 2 interactions.
	Action Decision	[OPT] <decision> How to fly from position <det>[[719,749,439,499,987]]</det> to position <det>[[352,470,439,499,499,998]]</det>, and provide a detailed plan.	Step1: Go straight, passing a brown irregular mid-rise building on the right and a red irregular mid-rise building on the left, until I reach above the trees. Step2: Continue straight ahead towards a blue-brown irregular mid-rise building, reaching above a parking lot...
	Task Scheduling	[OPT] <navigation>You need to formulate a flight plan for a quadcopter based on this map, enabling it to fly over all the buildings and reach the destination. The target location is described as follows: The white car parked perpendicular to a bright blue car in the parking lot on the right side of the West Midlands Police Custody Suite on Holford Drive. The three-dimensional coordinates of the landmark are as follows: <ref>West Midlands Police Custody Suite</ref><pos>[892, 208, 43]</pos> and <ref>Holford Drive</ref><pos>[580, 83, 30]</pos>. Your starting 3D coordinates and orientation angles are [866, 944, 554, 226, 829, 242]. You need to provide a series of three-dimensional waypoints and attitude angles for the quadcopter to reach the target location.	Step 1: Extract basic information as follows: Target: white car. Landmarks: Holford Drive, West Midlands Police Custody Suite. Surroundings: bright blue car, parking lot. Step 2: Get landmarks position: <ref>West Midlands Police Custody Suite</ref><pos>[892, 208, 43]</pos> and <ref>Holford Drive</ref><pos>[580, 83, 30]</pos>. Step 3: Get target position: <ref>white car</ref><pos>[798, 117, 22]</pos>. Step 4: Trajectory: <pos>[866, 944, 554, 226, 829, 242], ..., [801, 117, 27, 543, 821, 119]</pos>.

Figure 6: Clickable task examples are provided to users, covering eight different scenarios.

References

- [1] B. Lin, Y. Nie, Z. Wei, J. Chen, S. Ma, J. Han, H. Xu, X. Chang, and X. Liang, “Navcot: Boosting llm-based vision-and-language navigation via learning disentangled reasoning,” *IEEE Transactions on Pattern Analysis and Machine Intelligence*, vol. 47, no. 7, pp. 5945–5957, 2025.
- [2] Z. Yu, X. Ouyang, Z. Shao, M. Wang, and J. Yu, “Prophet: Prompting large language models with complementary answer heuristics for knowledge-based visual question answering,” *IEEE Transactions on Pattern Analysis and Machine Intelligence*, vol. 47, no. 8, pp. 6797–6808, 2025.
- [3] R. Xu, S. Yang, X. Wang, T. Wang, Y. Chen, J. Pang, and D. Lin, “Pointllm-v2: Empowering large language models to better understand point clouds,” *IEEE Transactions on Pattern Analysis and Machine Intelligence*, pp. 1–15, 2025.
- [4] D. Guo, D. Yang, H. Zhang, J. Song, R. Zhang, R. Xu, Q. Zhu, S. Ma, P. Wang, X. Bi *et al.*, “Deepseek-r1: Incentivizing reasoning capability in llms via reinforcement learning,” *arXiv preprint arXiv:2501.12948*, 2025.
- [5] D. Dai, C. Deng, C. Zhao, R. Xu, H. Gao, D. Chen, J. Li, W. Zeng, X. Yu, Y. Wu *et al.*, “Deepseekmoe: Towards ultimate expert specialization in mixture-of-experts language models,” *arXiv preprint arXiv:2401.06066*, 2024.
- [6] A. Liu, B. Feng, B. Wang, B. Liu, C. Zhao, C. Dengr, C. Ruan, D. Dai, D. Guo *et al.*, “Deepseek-v2: A strong, economical, and efficient mixture-of-experts language model,” *arXiv preprint arXiv:2405.04434*, 2024.
- [7] A. Liu, B. Feng, B. Xue, B. Wang, B. Wu, C. Lu, C. Zhao, C. Deng, C. Zhang, C. Ruan *et al.*, “Deepseek-v3 technical report,” *arXiv preprint arXiv:2412.19437*, 2024.
- [8] T. Brown, B. Mann, N. Ryder, M. Subbiah, J. D. Kaplan, P. Dhariwal, A. Neelakantan, P. Shyam, G. Sastry, A. Askell *et al.*, “Language models are few-shot learners,” *Advances in neural information processing systems*, vol. 33, pp. 1877–1901, 2020.
- [9] J. Achiam, S. Adler, S. Agarwal, L. Ahmad, I. Akkaya, F. L. Aleman, D. Almeida, J. Altenschmidt, S. Altman, S. Anadkat *et al.*, “Gpt-4 technical report,” *arXiv preprint arXiv:2303.08774*, 2023.
- [10] H. Touvron, T. Lavigra, G. Izacard, X. Martinet, M.-A. Lachaux, T. Lacroix, B. Rozière, N. Goyal, E. Hambro, F. Azhar *et al.*, “Llama: Open and efficient foundation language models,” *arXiv preprint arXiv:2302.13971*, 2023.

- [11] H. Touvron, L. Martin, K. Stone, P. Albert, A. Almahairi, Y. Babaei, N. Bashlykov, S. Batra, P. Bhargava, S. Bhosale *et al.*, “Llama 2: Open foundation and fine-tuned chat models,” *arXiv preprint arXiv:2307.09288*, 2023.
- [12] A. Grattafiori, A. Dubey, A. Jauhri, A. Pandey, A. Kadian, A. Al-Dahle, A. Letman, A. Mathur, A. Schelten, A. Vaughan *et al.*, “The llama 3 herd of models,” *arXiv preprint arXiv:2407.21783*, 2024.
- [13] X. Li, C. Wen, Y. Hu, Z. Yuan, and X. X. Zhu, “Vision-language models in remote sensing: Current progress and future trends,” *IEEE Geoscience and Remote Sensing Magazine*, 2024.
- [14] W. Zhang, M. Cai, T. Zhang, Y. Zhuang, and X. Mao, “Earthgpt: A universal multi-modal large language model for multi-sensor image comprehension in remote sensing domain,” *IEEE Transactions on Geoscience and Remote Sensing*, 2024.
- [15] W. Zhang, M. Cai, T. Zhang, G. Lei, Y. Zhuang, and X. Mao, “Popeye: A unified visual-language model for multi-source ship detection from remote sensing imagery,” *IEEE Journal of Selected Topics in Applied Earth Observations and Remote Sensing*, 2024.
- [16] J. D. Silva, J. Magalhães, D. Tuia, and B. Martins, “Large language models for captioning and retrieving remote sensing images,” *arXiv preprint arXiv:2402.06475*, 2024.
- [17] D. Muhtar, Z. Li, F. Gu, X. Zhang, and P. Xiao, “Lhrs-bot: Empowering remote sensing with vgi-enhanced large multimodal language model,” in *European Conference on Computer Vision*. Springer, 2024, pp. 440–457.
- [18] Y. Zhan, Z. Xiong, and Y. Yuan, “Skyeyegpt: Unifying remote sensing vision-language tasks via instruction tuning with large language model,” *ISPRS Journal of Photogrammetry and Remote Sensing*, vol. 221, pp. 64–77, 2025.
- [19] J. Luo, Z. Pang, Y. Zhang, T. Wang, L. Wang, B. Dang, J. Lao, J. Wang, J. Chen, Y. Tan *et al.*, “Skysensegpt: A fine-grained instruction tuning dataset and model for remote sensing vision-language understanding,” *arXiv preprint arXiv:2406.10100*, 2024.
- [20] K. Kuckreja, M. S. Danish, M. Naseer, A. Das, S. Khan, and F. S. Khan, “Geochat: Grounded large vision-language model for remote sensing,” in *Proceedings of the IEEE/CVF Conference on Computer Vision and Pattern Recognition*, 2024, pp. 27831–27840.
- [21] C. Pang, J. Wu, J. Li, Y. Liu, J. Sun, W. Li, X. Weng, S. Wang, L. Feng, G.-S. Xia *et al.*, “H2rsvlm: Towards helpful and honest remote sensing large vision language model,” *CoRR*, 2024.
- [22] P. Wang, H. Hu, B. Tong, Z. Zhang, F. Yao, Y. Feng, Z. Zhu, H. Chang, W. Diao, Q. Ye *et al.*, “Ringmogpt: A unified remote sensing foundation model for vision, language, and grounded tasks,” *IEEE Transactions on Geoscience and Remote Sensing*, 2024.
- [23] Y. Hu, J. Yuan, C. Wen, X. Lu, and X. Li, “Rsgpt: A remote sensing vision language model and benchmark,” *arXiv preprint arXiv:2307.15266*, 2023.
- [24] Y. Bazi, L. Bashmal, M. M. Al Rahhal, R. Ricci, and F. Melgani, “Rs-llava: A large vision-language model for joint captioning and question answering in remote sensing imagery,” *Remote Sensing*, vol. 16, no. 9, p. 1477, 2024.
- [25] J. Li, D. Li, S. Savarese, and S. Hoi, “Blip-2: Bootstrapping language-image pre-training with frozen image encoders and large language models,” in *International conference on machine learning*. PMLR, 2023, pp. 19730–19742.
- [26] W. Dai, J. Li, D. Li, A. Tiong, J. Zhao, W. Wang, B. Li, P. N. Fung, and S. Hoi, “Instructblip: Towards general-purpose vision-language models with instruction tuning,” *Advances in neural information processing systems*, vol. 36, pp. 49250–49267, 2023.
- [27] J. Chen, D. Zhu, X. Shen, X. Li, Z. Liu, P. Zhang, R. Krishnamoorthi, V. Chandra, Y. Xiong, and M. Elhoseiny, “Minigpt-v2: large language model as a unified interface for vision-language multi-task learning,” *arXiv preprint arXiv:2310.09478*, 2023.
- [28] Z. Peng, W. Wang, L. Dong, Y. Hao, S. Huang, S. Ma, and F. Wei, “Kosmos-2: Grounding multimodal large language models to the world,” *arXiv preprint arXiv:2306.14824*, 2023.
- [29] K. Chen, Z. Zhang, W. Zeng, R. Zhang, F. Zhu, and R. Zhao, “Shikra: Unleashing multimodal llm’s referential dialogue magic,” *arXiv preprint arXiv:2306.15195*, 2023.
- [30] X. Lai, Z. Tian, Y. Chen, Y. Li, Y. Yuan, S. Liu, and J. Jia, “Lisa: Reasoning segmentation via large language model,” in *Proceedings of the IEEE/CVF Conference on Computer Vision and Pattern Recognition*, 2024, pp. 9579–9589.
- [31] G. Team, R. Anil, S. Borgeaud, J.-B. Alayrac, J. Yu, R. Soricut, J. Schalkwyk, A. M. Dai, A. Hauth, K. Millican *et al.*, “Gemini: a family of highly capable multimodal models,” *arXiv preprint arXiv:2312.11805*, 2023.

[32] G. Team, P. Georgiev, V. I. Lei, R. Burnell, L. Bai, A. Gulati, G. Tanzer, D. Vincent, Z. Pan, S. Wang *et al.*, “Gemini 1.5: Unlocking multimodal understanding across millions of tokens of context,” *arXiv preprint arXiv:2403.05530*, 2024.

[33] G. Comanici, E. Bieber, M. Schaekermann, I. Pasupat, N. Sachdeva, I. Dhillon, M. Blistein, O. Ram, D. Zhang, E. Rosen *et al.*, “Gemini 2.5: Pushing the frontier with advanced reasoning, multimodality, long context, and next generation agentic capabilities,” *arXiv preprint arXiv:2507.06261*, 2025.

[34] A. Hurst, A. Lerer, A. P. Goucher, A. Perelman, A. Ramesh, A. Clark, A. Ostrow, A. Welihinda, A. Hayes, A. Radford *et al.*, “Gpt-4o system card,” *arXiv preprint arXiv:2410.21276*, 2024.

[35] OpenAI, “Gpt-4o mini: advancing cost-efficient intelligence,” Online, 2024, available: <https://openai.com/zh-Hans-CN/index/gpt-4o-mini-advancing-cost-efficient-intelligence/>.

[36] J. Bai, S. Bai, S. Yang, S. Wang, S. Tan, P. Wang, J. Lin, C. Zhou, and J. Zhou, “Qwen-vl: A versatile vision-language model for understanding, localization, text reading, and beyond,” *arXiv preprint arXiv:2308.12966*, 2023.

[37] P. Wang, S. Bai, S. Tan, S. Wang, Z. Fan, J. Bai, K. Chen, X. Liu, J. Wang, W. Ge *et al.*, “Qwen2-vl: Enhancing vision-language model’s perception of the world at any resolution,” *arXiv preprint arXiv:2409.12191*, 2024.

[38] Y. C. Shuai Bai and R. C. et al., “Qwen3-vl technical report,” *arXiv preprint arXiv:2511.21631*, 2025.

[39] L. Wang, H. Gao, C. Zhao, X. Sun, and D. Dai, “Auxiliary-loss-free load balancing strategy for mixture-of-experts,” *arXiv preprint arXiv:2408.15664*, 2024.

[40] Z. Wu, X. Chen, Z. Pan, X. Liu, W. Liu, D. Dai, H. Gao, Y. Ma, C. Wu, B. Wang *et al.*, “Deepseek-vl2: Mixture-of-experts vision-language models for advanced multimodal understanding,” *arXiv preprint arXiv:2412.10302*, 2024.

[41] L. Wang, C. Ma, X. Feng, Z. Zhang, H. Yang, J. Zhang, Z. Chen, J. Tang, X. Chen, Y. Lin *et al.*, “A survey on large language model based autonomous agents,” *Frontiers of Computer Science*, vol. 18, no. 6, p. 186345, 2024.

[42] N. Shinn, F. Cassano, A. Gopinath, K. Narasimhan, and S. Yao, “Reflexion: Language agents with verbal reinforcement learning,” *Advances in Neural Information Processing Systems*, vol. 36, pp. 8634–8652, 2023.

[43] Y. Shen, K. Song, X. Tan, D. Li, W. Lu, and Y. Zhuang, “Hugginggpt: Solving ai tasks with chatgpt and its friends in hugging face,” *Advances in Neural Information Processing Systems*, vol. 36, pp. 38 154–38 180, 2023.

[44] T. Schick, J. Dwivedi-Yu, R. Dessì, R. Raileanu, M. Lomeli, E. Hambro, L. Zettlemoyer, N. Cancedda, and T. Scialom, “Toolformer: Language models can teach themselves to use tools,” *Advances in Neural Information Processing Systems*, vol. 36, pp. 68 539–68 551, 2023.

[45] S. Hong, M. Zhuge, J. Chen, X. Zheng, Y. Cheng, J. Wang, C. Zhang, Z. Wang, S. K. S. Yau, Z. Lin *et al.*, “Metagpt: Meta programming for a multi-agent collaborative framework,” in *The Twelfth International Conference on Learning Representations*, 2023.

[46] H. Hu, P. Wang, H. Bi, B. Tong, Z. Wang, W. Diao, H. Chang, Y. Feng, Z. Zhang, Y. Wang *et al.*, “Rs-vheat: Heat conduction guided efficient remote sensing foundation model,” in *Proceedings of the IEEE/CVF International Conference on Computer Vision*, 2025, pp. 9876–9887.

[47] H. Bi, Y. Feng, B. Tong, M. Wang, H. Yu, Y. Mao, H. Chang, W. Diao, P. Wang, Y. Yu, H. Peng, Y. Zhang, K. Fu, and X. Sun, “Ringmoe: Mixture-of-modality-experts multi-modal foundation models for universal remote sensing image interpretation,” *IEEE Transactions on Pattern Analysis and Machine Intelligence*, pp. 1–18, 2025.

[48] Y. Zhan, Z. Xiong, and Y. Yuan, “Rsvg: Exploring data and models for visual grounding on remote sensing data,” *IEEE Transactions on Geoscience and Remote Sensing*, vol. 61, pp. 1–13, 2023.

[49] F. Liu, D. Chen, Z. Guan, X. Zhou, J. Zhu, Q. Ye, L. Fu, and J. Zhou, “Remoteclip: A vision language foundation model for remote sensing,” *IEEE Transactions on Geoscience and Remote Sensing*, 2024.

[50] F. Yao, Y. Yue, Y. Liu, X. Sun, and K. Fu, “Aeroverse: Uav-agent benchmark suite for simulating, pre-training, finetuning, and evaluating aerospace embodied world models,” *arXiv preprint arXiv:2408.15511*, 2024.

[51] S. Lobry, D. Marcos, J. Murray, and D. Tuia, “Rsvqa: Visual question answering for remote sensing data,” *IEEE Transactions on Geoscience and Remote Sensing*, vol. 58, no. 12, pp. 8555–8566, 2020.

[52] G.-S. Xia, J. Hu, F. Hu, B. Shi, X. Bai, Y. Zhong, L. Zhang, and X. Lu, “Aid: A benchmark data set for performance evaluation of aerial scene classification,” *IEEE Transactions on Geoscience and Remote Sensing*, vol. 55, no. 7, pp. 3965–3981, 2017.

[53] K. Li, G. Wan, G. Cheng, L. Meng, and J. Han, “Object detection in optical remote sensing images: A survey and a new benchmark,” *ISPRS journal of photogrammetry and remote sensing*, vol. 159, pp. 296–307, 2020.

[54] G.-S. Xia, X. Bai, J. Ding, Z. Zhu, S. Belongie, J. Luo, M. Datcu, M. Pelillo, and L. Zhang, “Dota: A large-scale dataset for object detection in aerial images,” in *Proceedings of the IEEE conference on computer vision and pattern recognition*, 2018, pp. 3974–3983.

[55] F. Wang, H. Wang, Z. Guo, D. Wang, Y. Wang, M. Chen, Q. Ma, L. Lan, W. Yang, J. Zhang *et al.*, “Xlrs-bench: Could your multimodal llms understand extremely large ultra-high-resolution remote sensing imagery?” in *Proceedings of the Computer Vision and Pattern Recognition Conference*, 2025, pp. 14 325–14 336.

[56] X. Li, J. Ding, and M. Elhoseiny, “Vrsbench: A versatile vision-language benchmark dataset for remote sensing image understanding,” *Advances in Neural Information Processing Systems*, vol. 37, pp. 3229–3242, 2024.

[57] J. Lee, T. Miyanishi, S. Kurita, K. Sakamoto, D. Azuma, Y. Matsuo, and N. Inoue, “Citynav: A large-scale dataset for real-world aerial navigation,” in *Proceedings of the IEEE/CVF International Conference on Computer Vision*, 2025, pp. 5912–5922.

[58] G. Cheng, J. Han, P. Zhou, and L. Guo, “Multi-class geospatial object detection and geographic image classification based on collection of part detectors,” *ISPRS Journal of Photogrammetry and Remote Sensing*, vol. 98, pp. 119–132, 2014.

[59] Y. Li, X. Li, W. Li, Q. Hou, L. Liu, M.-M. Cheng, and J. Yang, “Sardet-100k: Towards open-source benchmark and toolkit for large-scale sar object detection,” *arXiv preprint arXiv:2403.06534*, 2024.

[60] B. Qu, X. Li, D. Tao, and X. Lu, “Deep semantic understanding of high resolution remote sensing image,” in *2016 International conference on computer, information and telecommunication systems (Cits)*. IEEE, 2016, pp. 1–5.

[61] X. Lu, B. Wang, X. Zheng, and X. Li, “Exploring models and data for remote sensing image caption generation,” *IEEE Transactions on Geoscience and Remote Sensing*, vol. 56, no. 4, pp. 2183–2195, 2017.

[62] Q. Cheng, H. Huang, Y. Xu, Y. Zhou, H. Li, and Z. Wang, “Nwpucaptions dataset and mlca-net for remote sensing image captioning,” *IEEE Transactions on Geoscience and Remote Sensing*, vol. 60, pp. 1–19, 2022.

[63] G. Cheng, J. Han, and X. Lu, “Remote sensing image scene classification: Benchmark and state of the art,” *Proceedings of the IEEE*, vol. 105, no. 10, pp. 1865–1883, 2017.

[64] G.-S. Xia, W. Yang, J. Delon, Y. Gousseau, H. Sun, and H. Maître, “Structural high-resolution satellite image indexing,” in *ISPRS TC VII Symposium-100 Years ISPRS*, vol. 38, 2010, pp. 298–303.

[65] Y. Yang and S. Newsam, “Bag-of-visual-words and spatial extensions for land-use classification,” in *Proceedings of the 18th SIGSPATIAL international conference on advances in geographic information systems*, 2010, pp. 270–279.

[66] X. Sun, Q. Yan, C. Deng, C. Liu, Y. Jiang, Z. Hou, W. Lu, F. Yao, X. Liu, L. Hao *et al.*, “Recon1m: A large-scale benchmark dataset for relation comprehension in remote sensing imagery,” *arXiv preprint arXiv:2406.06028*, 2024.

[67] J. Suo, T. Wang, X. Zhang, H. Chen, W. Zhou, and W. Shi, “Hit-uav: A high-altitude infrared thermal dataset for unmanned aerial vehicle-based object detection,” *Scientific Data*, vol. 10, no. 1, p. 227, 2023.

[68] Raytron Technology Co., Ltd., “Sea-shipping,” Online, 2021, available: https://openai.raytrontek.com/apply/Sea_shipping.html/.

[69] ———, “Infrared-security,” Online, 2021, available: https://openai.raytrontek.com/apply/Infrared_security.html/.

[70] ———, “Aerial-mancar,” Online, 2021, available: http://openai.raytrontek.com/apply/Aerial_mancar.html/.

[71] ———, “Double-light-vehicle,” Online, 2021, available: http://openai.raytrontek.com/apply/Double_light_vehicle.html/.

[72] Center for Optics Research and Engineering of Shandong University, “Oceanic-ship,” Online, 2020, available: <http://www.core.sdu.edu.cn/info/1133/2174.htm>.

[73] X. Zhai, B. Mustafa, A. Kolesnikov, and L. Beyer, “Sigmoid loss for language image pre-training,” in *Proceedings of the IEEE/CVF international conference on computer vision*, 2023, pp. 11 975–11 986.

[74] E. J. Hu, Y. Shen, P. Wallis, Z. Allen-Zhu, Y. Li, S. Wang, L. Wang, W. Chen *et al.*, “Lora: Low-rank adaptation of large language models.” *ICLR*, vol. 1, no. 2, p. 3, 2022.

[75] H. Li, X. Dou, C. Tao, Z. Wu, J. Chen, J. Peng, M. Deng, and L. Zhao, “Rsi-cb: A large-scale remote sensing image classification benchmark using crowdsourced data,” *Sensors*, vol. 20, no. 6, p. 1594, 2020.

[76] Q. Zou, L. Ni, T. Zhang, and Q. Wang, “Deep learning based feature selection for remote sensing scene classification,” *IEEE Geoscience and Remote Sensing Letters*, vol. 12, no. 11, pp. 2321–2325, 2015.

- [77] P. Zhang, Y. Bai, D. Wang, B. Bai, and Y. Li, “Few-shot classification of aerial scene images via meta-learning,” *Remote Sensing*, vol. 13, no. 1, p. 108, 2020.
- [78] W. Zhou, S. Newsam, C. Li, and Z. Shao, “Patternnet: A benchmark dataset for performance evaluation of remote sensing image retrieval,” *ISPRS journal of photogrammetry and remote sensing*, vol. 145, pp. 197–209, 2018.
- [79] D. Hou, Z. Miao, H. Xing, and H. Wu, “Two novel benchmark datasets from arcgis and bing world imagery for remote sensing image retrieval,” *International Journal of Remote Sensing*, vol. 42, no. 1, pp. 240–258, 2021.
- [80] P. Anderson, Q. Wu, D. Teney, J. Bruce, M. Johnson, N. Sünderhauf, I. Reid, S. Gould, and A. Van Den Hengel, “Vision-and-language navigation: Interpreting visually-grounded navigation instructions in real environments,” in *Proceedings of the IEEE conference on computer vision and pattern recognition*, 2018, pp. 3674–3683.
- [81] S. Liu, H. Zhang, Y. Qi, P. Wang, Y. Zhang, and Q. Wu, “Aerialvln: Vision-and-language navigation for uavs,” in *Proceedings of the IEEE/CVF International Conference on Computer Vision*, 2023, pp. 15 384–15 394.
- [82] D. Zhu, J. Chen, X. Shen, X. Li, and M. Elhoseiny, “Minigpt-4: Enhancing vision-language understanding with advanced large language models,” *arXiv preprint arXiv:2304.10592*, 2023.
- [83] X. Lu, B. Wang, and X. Zheng, “Sound active attention framework for remote sensing image captioning,” *IEEE Transactions on Geoscience and Remote Sensing*, vol. 58, no. 3, pp. 1985–2000, 2019.
- [84] G. Hoxha, G. Scuccato, and F. Melgani, “Improving image captioning systems with postprocessing strategies,” *IEEE Transactions on Geoscience and Remote Sensing*, vol. 61, pp. 1–13, 2023.
- [85] H. Liu, C. Li, Q. Wu, and Y. J. Lee, “Visual instruction tuning,” *Advances in neural information processing systems*, vol. 36, 2024.
- [86] Z. Yuan, L. Mou, Q. Wang, and X. X. Zhu, “From easy to hard: Learning language-guided curriculum for visual question answering on remote sensing data,” *IEEE transactions on geoscience and remote sensing*, vol. 60, pp. 1–11, 2022.
- [87] Y. Bazi, M. M. Al Rahhal, M. L. Mekhalfi, M. A. Al Zuair, and F. Melgani, “Bi-modal transformer-based approach for visual question answering in remote sensing imagery,” *IEEE Transactions on Geoscience and Remote Sensing*, vol. 60, pp. 1–11, 2022.
- [88] Z. Zhang, L. Jiao, L. Li, X. Liu, P. Chen, F. Liu, Y. Li, and Z. Guo, “A spatial hierarchical reasoning network for remote sensing visual question answering,” *IEEE Transactions on Geoscience and Remote Sensing*, vol. 61, pp. 1–15, 2023.
- [89] Q. Ye, H. Xu, J. Ye, M. Yan, A. Hu, H. Liu, Q. Qian, J. Zhang, and F. Huang, “mplug-owl2: Revolutionizing multi-modal large language model with modality collaboration,” in *Proceedings of the ieee/cvf conference on computer vision and pattern recognition*, 2024, pp. 13 040–13 051.
- [90] H. Liu, C. Li, Y. Li, and Y. J. Lee, “Improved baselines with visual instruction tuning,” in *Proceedings of the IEEE/CVF Conference on Computer Vision and Pattern Recognition*, 2024, pp. 26 296–26 306.
- [91] Q. Bi, K. Qin, H. Zhang, and G.-S. Xia, “Local semantic enhanced convnet for aerial scene recognition,” *IEEE Transactions on Image Processing*, vol. 30, pp. 6498–6511, 2021.
- [92] O. Manas, A. Lacoste, X. Giró-i Nieto, D. Vazquez, and P. Rodriguez, “Seasonal contrast: Unsupervised pre-training from uncurated remote sensing data,” in *Proceedings of the IEEE/CVF International Conference on Computer Vision*, 2021, pp. 9414–9423.
- [93] A. Radford, J. W. Kim, C. Hallacy, A. Ramesh, G. Goh, S. Agarwal, G. Sastry, A. Askell, P. Mishkin, J. Clark *et al.*, “Learning transferable visual models from natural language supervision,” in *International conference on machine learning*. PMLR, 2021, pp. 8748–8763.